Liu, T. *et al*. (2024). *Géotechnique* **74**, No. 6, 540–552 [https://doi.org/10.1680/jgeot.21.00199]

An experimental investigation into the behaviour of destructured chalk under cyclic loading

TINGFA LIU*, REZA AHMADI-NAGHADEH†, KEN VINCK‡, RICHARD J. JARDINE§, STAVROULA KONTOE||, RÓISÍN M. BUCKLEY¶ and BYRON W. BYRNE**

Low-to-medium-density chalk can be destructured to soft putty by high-pressure compression, dynamic impact or large-strain repetitive shearing. These process all occur during pile driving and affect subsequent static and cyclic load-carrying capacities. This paper reports undrained triaxial experiments on destructured chalk, which show distinctly time-dependent behaviour as well as highly non-linear stiffness, well-defined phase transformation and stable ultimate critical states under monotonic loading. The chalk's response to high-level undrained cyclic loading invokes both contractive and dilative phases that lead to pore pressure build-up, leftward effective stress path drift, permanent strain accumulation, cyclic stiffness losses and increasing damping ratios that resemble those of silts. These outcomes are relatively insensitive to consolidation pressures and are distinctly different to those of the parent intact chalk. The maximum number of cycles that can be sustained under given combinations of mean and cyclic stresses are expressed in an interactive stress diagram which also identifies conditions under which cycling has no deleterious effect. Empirical correlations are proposed to predict the number of cycles to failure and mean effective stress drift trends under the most critical cyclic conditions. Specimens that survive long-term cycling present higher post-cyclic stiffnesses and shear strengths than equivalent 'virgin' specimens.

KEYWORDS: chalk putty; cyclic loading; destructuration; triaxial; laboratory testing

INTRODUCTION

Chalk is a very soft biomicrite composed of silt-sized crushable calcium carbonate ($CaCO_3$) aggregates. Vinck *et al*. (2022) demonstrate how low-to-medium-density chalks (with intact dry densities, IDD $< 1{\cdot}70$ Mg/m^3) develop stiff, brittle and ultimately dilative behaviour when sheared from in situ effective stress levels. However, their mechanical properties degrade markedly under dynamic, cyclic or high-pressure shearing, with important implications for problems such as the design of driven piles (Carrington *et al*., 2011; Diambra *et al*., 2014; Carotenuto *et al*., 2018; Buckley *et al*., 2020a).

Impact driving creates low-strength, destructured, chalk putty beneath the piles' advancing tips, which spreads and further softens around their shafts. Buckley *et al*. (2018) and Vinck (2021) identified how destructuration varied with radial distance from the axes of open steel piles at shallow depths (above the water table), considering conditions after driving, and after long-term ageing and load testing. The thin annuli of putty formed around shafts on driving provided average driving resistances ≈ 20 kPa and reconsolidated over time to achieve notably lower water contents and significantly greater shear strengths. The response of the reconsolidated putty to monotonic and cyclic loading, as well as interface shear, is central to addressing axial capacity and cyclic loading performance for piles driven in chalk.

This paper explores the cyclic behaviour of reconsolidated destructured chalk. Stress-controlled cyclic triaxial tests are reported on material from the 'axial–lateral pile analysis for chalk applying multi-scale field and laboratory testing' (ALPACA) project's St Nicholas-at-Wade (SNW), UK pile research site, whose geotechnical profile and chalk properties are described by Vinck (2021). The destructured chalk's response to undrained cycling is interpreted with reference to those of saturated silts and silty sands, as reported by Carraro *et al*. (2003), Mao & Fahey (2003), Hyde *et al*. (2006), Sanin & Wijewickreme (2006), Sağlam & Bakır (2014) and Wei & Yang (2019). Ahmadi-Naghadeh *et al*. (2022) report parallel research into the intact chalk's cyclic response under similar cycling, identifying behaviour that differs starkly from that of unbonded soils and compares more closely with that of rocks, concretes or metals. Bialowas *et al*. (2018) and Alvarez-Borges *et al*. (2018, 2020) report earlier testing on reconstituted SNW chalk.

CHALK PUTTY FORMED BY DYNAMIC COMPACTION

Laboratory dynamic compaction, applied at in situ water content, destructures low-to-medium-density chalk in an analogous way to pile driving (Doughty *et al*., 2018) and provides uniform batches for laboratory testing. Puttified

Manuscript received 14 July 2021; revised manuscript accepted 12 January 2022. First published online ahead of print 14 March 2022.
Discussion on this paper closes on 1 September 2024, for further details see p. ii.
Published with permission by Emerald Publishing Limited under the CC-BY 4.0 license. (http://creativecommons.org/licenses/by/4.0/)
* Department of Civil Engineering, University of Bristol, Bristol, UK; formerly Department of Civil and Environmental Engineering, Imperial College London, London, UK (Orcid:0000-0002-5719-8420).
† Formerly Department of Civil and Environmental Engineering, Imperial College London, London, UK; now Department of Construction Engineering and Lighting Science, School of Engineering, Jönköping University, Jönköping, Sweden (Orcid:0000-0002-2215-441X).
‡ Department of Civil and Environmental Engineering, Imperial College London, London, UK (Orcid:0000-0002-0990-0895).
§ Department of Civil and Environmental Engineering, Imperial College London, London, UK (Orcid:0000-0001-7147-5909).
|| Department of Civil and Environmental Engineering, Imperial College London, London, UK (Orcid:0000-0002-8354-8762).
¶ School of Engineering, University of Glasgow, Glasgow, UK (Orcid:0000-0001-5152-7759).
** Department of Engineering Science, Oxford University, Oxford, UK (Orcid:0000-0002-9704-0767).

Downloaded by [] on [30/05/24]. Published with permission by the ICE under the CC-BY license

specimens were formed for this study through compaction of block samples preserved from 1·4 m depth, whose unconfined compression strengths (UCS) exceeded 3 MPa, despite their 29–30% initial natural water contents. Up to 150 blows were applied at ≈2 s intervals with a 4·5 kg ram and 300 mm drop height to intact lumps contained in a 100 mm dia. mould to produce ≈0·3 litre batches of chalk putty. Mixing every 50 blows ensured uniformity, and the process, which took ≈10 min, involved slight drying with ≈1% water contents reductions. Index testing indicated 9 ± 3 kPa fall-cone undrained shear strengths, liquid and plastic limits of 30·6% and 24·2%, respectively, grain specific gravity $G_s = 2{\cdot}71$ and median grain size $D_{50} \approx 3{\cdot}0$ μm.

Figure 1 presents constant-rate-of-strain (CRS; at 0·6%/h) oedometer compression curves for intact and destructured putty chalk samples. Also shown is a test on samples reconstituted by re-hydrating pulverised dried chalk to 1·4 times the liquid limit. The intact and reconstituted compression (NCL*) oedometer curves of natural clays reflect their different structures (Burland, 1990). Smith *et al.* (1992) employed the ratio of the intact soil's vertical effective stress at yield σ'_{vy} to that projected onto the reconstituted curve at the same void ratio as a scalar 'oedometer sensitivity' measure of the clay's structure. Fig. 1 indicates an oedometer 'sensitivity' of ≈24 for the natural chalk. The intact chalk shows $S_u \approx 1{\cdot}2$ MPa at this depth (Vinck *et al.*, 2022), which suggests a higher undrained shear strength sensitivity ≈130. The intact CRS trace suggests that oedometer sensitivity declines towards unity as pressures increase post-yield and the e–σ'_v trace curves towards the NCL* whose compression index $C_c^* = 0{\cdot}18$. The fully destructured putty starts at a lower liquidity index than the reconstituted chalk, but follows a similar trend once $\sigma'_v > 50$ kPa, falling far below the intact sample's curve, although exhibiting similar unloading curves and swelling indices $C_s \approx 0{\cdot}01$. The putty exhibited markedly time-dependent one-dimensional (1D) compression behaviour in parallel stage loaded oedometer tests that gave secondary compression coefficients $C_{\alpha e} = \Delta e / \Delta \log_{10}(t) = 0{\cdot}003$ over the $100 < \sigma'_v < 400$ kPa range and a $C_{\alpha e}/C_c = 0{\cdot}06$ ratio, which is remarkably high for an inorganic soil (Mesri & Vardhanabhuti, 2006). As shown later, triaxial specimens prepared from the putty developed significant volumetric strains under relatively modest isotropic consolidation stresses and attained specific volume–mean effective stress (v–p') states well below (or 'dryer than') the destructured chalk followed in its CRS oedometer test. These findings and related features are discussed later in relation to the state parameter framework for sands (Been & Jefferies, 1985).

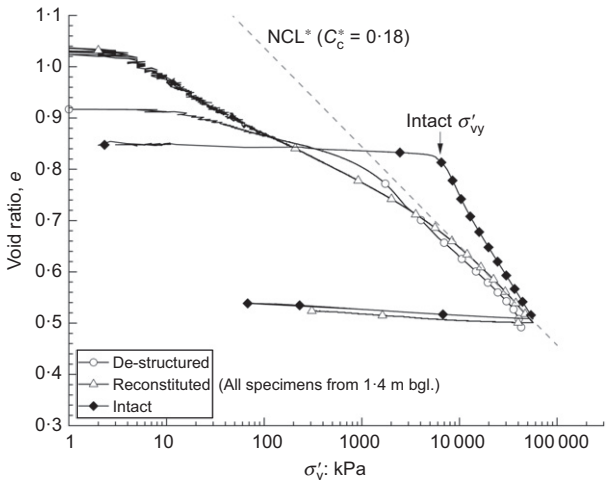


Fig. 1. One-dimensional compression behaviour of destructured (puttified), reconstituted and intact chalk established from CRS (constant rate of strain; 0·6%/h) tests

TRIAXIAL TESTING ON PUTTY SAMPLES

Apparatus and procedures

Cyclic triaxial tests were performed with automated hydraulic stress-path apparatus. A suction cap and half-ball connection system helped to align the (initially soft) specimens with the load cells and minimise tilting and bedding. Layered latex discs and high-vacuum grease deployed at the specimen tops and bottoms reduced end constraint. Putty was placed in 5–10 g increments into a split mould, lined with a latex membrane, pre-set on the triaxial base platen. Care was taken to eliminate macro-voids and produce uniform 38 mm dia., 80 mm high, specimens with flat ends, topped with poly (methyl methacrylate) (PMMA) caps. The soft specimens' ability to maintain regular shapes and resist disturbance during mould dismantling and instrumenting was improved through an 'in-mould' isotropic consolidation stage implemented by maintaining a triaxial cell-to-back-pressure difference of 70 kPa for 15 h under drained conditions, which led to volume strains of ≈10%. The resulting, relatively robust, specimens' dimensions were then measured and sets of linear variable differential transducer (LVDT) local strain sensors were mounted, including a radial-strain belt.

The specimens were saturated by applying 300–400 kPa back-pressure, maintaining $p' = 20$ kPa until $B > 0{\cdot}97$, followed by isotropic consolidation at 1 kPa/min to reach the targeted mean effective stresses (p'_0), which led to average $C_{\alpha e}$ values (0·0034 and 0·0046) under p' levels of 200 and 400 kPa, respectively. Creep periods of 8–12 days allowed residual axial straining to diminish to < 0·005%/day, 1000 times lower than the 5%/day applied in subsequent monotonic shearing stages. Samples consolidated to $p'_0 = 200$ kPa and 400 kPa had post-creep (pre-shearing) void ratios of 0·63 and 0·59, respectively, corresponding to water contents (23·3% and 21·8%) that, as noted in the putty zone around driven pile shafts, fell well below those of the undisturbed intact chalk and far below the oedometer curves shown in Fig. 1.

Test programme and code

Five monotonic 'control' tests characterised the putty's response to undrained shearing (at 5% axial strain/day) after isotropic consolidation to $p'_0 = 70$, 200 and 400 kPa followed by drained creep, that aimed to match the medium to high range of radial effective stresses ($10 < \sigma'_{rf} < 500$ kPa) interpreted around the ALPACA pile shafts after full ageing (Buckley *et al.*, 2020b). Specimen details and testing conditions are outlined in Table 1.

The subsequent cyclic programme focused mainly on 11 tests at $p'_0 = 200$ kPa, supplemented by four experiments cycled from $p'_0 = 400$ kPa with, naturally, lower initial void ratios. Cell pressures were held constant, while deviator stresses varied sinusoidally about a fixed q_{mean} by the amplitudes q_{cyc} listed in Table 2. Note that $q = (\sigma'_v - \sigma'_h)$ and $p' = (\sigma'_v + 2\sigma'_h)/3$, and that q_{mean} and q_{cyc} are also shown as ratios of the putty chalk's p'_0 and $2S_u$ values to aid interpretation. Relatively long periods of 300 s were adopted to enable full control, pore-pressure equalisation and detailed logging of all parameters. Recalling the material's time-dependent compression behaviour, the triaxial tests may overestimate the degree to which cycling

Downloaded by [] on [30/05/24]. Published with permission by the ICE under the CC-BY license

Table 1. Summary of undrained monotonic triaxial tests: maximum Young's moduli, stress conditions and the corresponding axial strains (in brackets) at phase transformation (PT) and ultimate states

Test	e*	p'_0: kPa	E^u_{max}: MPa	$\left(\frac{E^u_{max}}{p_{ref}}\right)\Big/\dagger\left(\frac{p'_0}{p_{ref}}\right)^{0.5}$	$q_{(PT)}$: kPa (ε_a: %)	$p'_{(PT)}$: kPa	$q_{(ult)}$: kPa (ε_a: %)	$p'_{(ult)}$: kPa	$(q/p')_{ult}$	ϕ'_{ult} degrees
DM-C1	0·714	70	643·1	7637·0	42·6 (0·6%)	39·9	309·7 (30·9%)	229·4	1·35	31·6
DM-C2	0·648	200	1195·3	8397·6	106·1 (1·4%)	100·3	606·1 (24·0%)	480·8	1·26	
DM-C3	0·606	400	1472·5	7315·1	208·9 (1·2%)	198·3	1618·5 (25·0%)	1273·0	1·27	
DM-E1	0·609	200	1114·1	7827·2	−132·1 (−1·1%)	149·1	−207·4 (−7·0%)	233·4	−0·89	30·1
DM-E2	0·580	400	1393·1	6920·7	−256·9 (−1·0%)	319·9	−364·2 (−7·0%)	453·9	−0·80	

*Void ratio prior to undrained shearing; calculated based on post-test water content measurements.
†p_{ref}, reference pressure (101·3 kPa).

Table 2. Summary of cyclic triaxial test conditions and parameters

Test	e*	q_{mean}: kPa	$q_{mean}/(2S_u)$	q_{cyc}: kPa	$q_{cyc}/(2S_u)$	q_{max}: kPa	$q_{max}/(2S_u)$	q_{mean}/p'_0	q_{cyc}/p'_0
DCy-A1	0·644	0	0	30	0·30	30	0·30	0	0·15
DCy-B1	0·607	0	0	45	0·45	45	0·45	0	0·23
DCy-C1	0·615	30	0·30	30	0·30	60	0·60	0·15	0·15
DCy-C2	0·621	15	0·15	45	0·45	60	0·60	0·08	0·23
DCy-C3	0·659	0	0	60	0·60	60	0·60	0	0·30
DCy-CX	0·616	−15	−0·15	45	0·45	−60	−0·60	−0·08	0·23
DCy-D1	0·621	79	0·79	17	0·17	96	0·96	0·40	0·09
DCy-D2	0·675	57	0·57	30	0·30	87	0·87	0·29	0·15
DCy-D3	0·648	44	0·44	44	0·44	88	0·88	0·22	0·22
DCy-D4	0·621	28	0·28	60	0·60	88	0·88	0·14	0·30
DCy-D5	0·591	0	0	75	0·75	75	0·75	0	0·38
DCy-A1-E	0·620	0	0	60	0·30	60	0·30	0	0·15
DCy-B1-E	0·587	0	0	90	0·45	90	0·45	0	0·23
DCy-C3-E	0·597	0	0	120	0·60	120	0·60	0	0·30
DCy-D5-E	0·575	0	0	150	0·75	150	0·75	0	0·38

*Void ratio prior to undrained monotonic pre-shearing or cyclic shearing; calculated based on post-test water content measurements.

affects offshore structures under typically shorter (perhaps 10 s) period cyclic loading. Each test's code is composed as

(*a*) letter 'D' denotes destructured chalk
(*b*) letter 'M' signifies monotonic and letters 'Cy' indicate cyclic loading
(*c*) group letters A, B, C or D signify the level of maximum q applied, in ascending order
(*d*) a numeral signifies the applied q_{cyc} level in the A to D groups, in ascending order; letter 'X' represents the single case where negative q_{mean} was applied
(*e*) letter 'E' signifies the test series performed at the elevated p'_0 of 400 kPa.

MONOTONIC TESTS

The putty's response to undrained triaxial compression (TXC) and extension (TXE) is displayed in Fig. 2, plotting zoomed-in q–p' effective stress paths and deviatoric stress (q)–axial strain (ε_a) trends over the small to medium strain range. Specimens exhibited broadly linear elastic behaviour up to ε_a limits of 0·002% and 0·003% for the $p'_0 = 200$ and 400 kPa tests, respectively, corresponding to increments $\Delta q \approx 23{\cdot}1$ and 43·0 kPa with an average $\Delta q/(2S_u) \approx 0{\cdot}22$. The q–p' effective stress paths rose nearly vertically upon compression and extension, suggesting that the re-consolidated (mildly aged) putty's initial stiffness response was largely isotropic (Vinck *et al.*, 2022).

The effective stress paths rotated to follow leftward (contractive) stages after mobilising modest 'peak' resistances (after relatively small strains, $\varepsilon_a < 0{\cdot}2\%$) and showed strain softening as shearing continued up to phase transformation (PT) points at which their paths rotated abruptly and climbed towards ultimate (critical state) conditions (see Table 1). Continued straining led to markedly higher ultimate strengths as the specimens attempted to dilate from their states positioned well below the normal compression line indicated in Fig. 1.

As discussed later, the chalk putty's resistance to cyclic loading is dominated by its pre-PT behaviour. The peak pre-PT $q_{(PT)}$ points were taken as indicating the operational monotonic shear strengths ($2S_u$), giving rounded S_u values of 50 kPa and 100 kPa for the $p'_0 = 200$ and 400 kPa tests, respectively, with $S_u/p'_0 = 0{\cdot}25$. Specimens undergoing extension developed similarly contractive pre-PT responses to shearing, followed by dilation after reaching PT, giving broadly similar, yet not fully symmetric stress paths and shear strengths to the compression tests, despite their different σ_1 directions and $b = (\sigma_2 - \sigma_3)/(\sigma_1 - \sigma_3)$ ratios (or Lode angles θ). While the isotropically consolidated putty did not manifest any significant combined effect of anisotropy or b ratio on its pre-PT shearing behaviour, the extension tests' dilative post-PT stages were truncated prematurely by localised necking from $\varepsilon_a \approx -7{\cdot}5\%$ onwards that obscured any trend towards stable ultimate critical states.

Table 1 summarises the specimens' linear elastic (maximum) Young's moduli (E^u_{max}), their PT stress points, large-strain ultimate (critical state) states and the corresponding strains. The q/p' ratios at PT, critical state (in compression) and ultimate failure in extension in the (inherently more reliable) higher pressure tests were 1·05, 1·27 and 0·86, respectively. The latter two ratios both correspond to $\phi'_{cs} \approx 31°$, matching the angle found in high-pressure tests on intact samples.

Downloaded by [] on [30/05/24]. Published with permission by the ICE under the CC-BY license

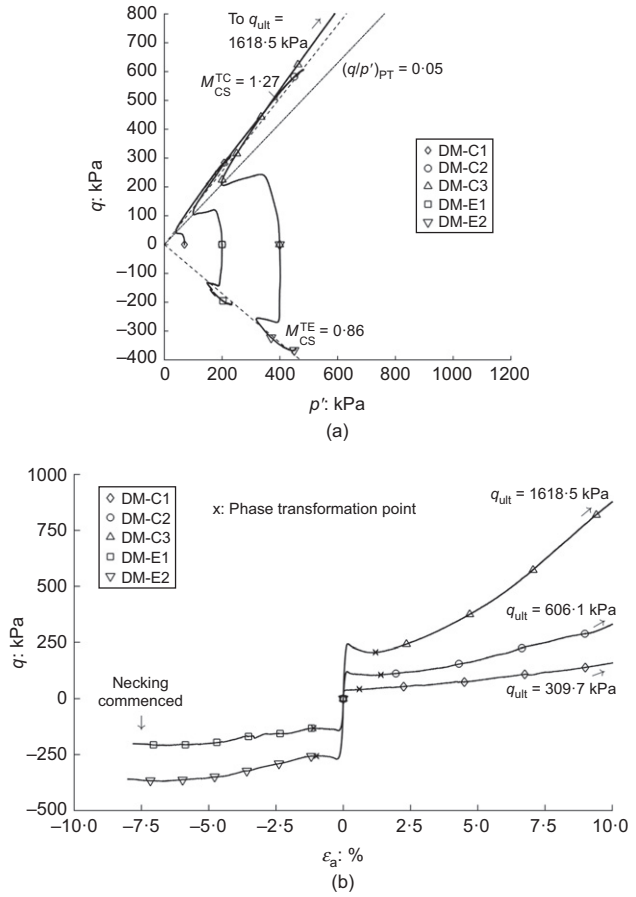


Fig. 2. Triaxial compression and extension behaviour of puttified chalk: (a) effective stress paths; (b) deviatoric stress–axial strain response (see also details in Table 1)

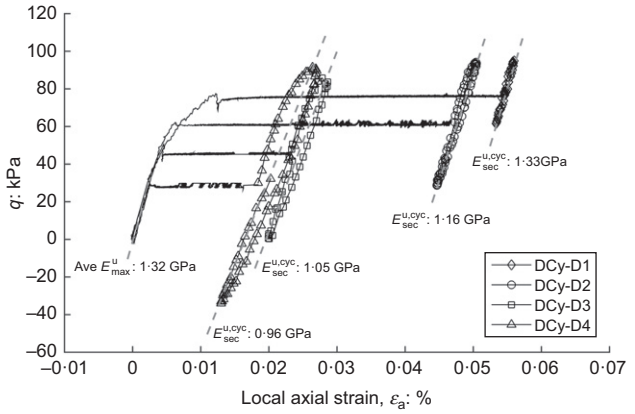


Fig. 3. Deviatoric stress–axial strain responses for tests DCy-D1 to DCy-D4 during monotonic pre-shearing, creep and first cycle, also indicating average maximum Young's modulus in pre-shearing and secant cyclic moduli for the first peak-to-trough half cycle

CYCLIC TESTING PROCEDURES AND FAILURE CRITERIA

As listed in Table 2, the cyclic triaxial experiments investigated a range of one- and two-way q_{mean}, q_{cyc} and q_{max} conditions, including cycling into extension. The elevated pressure ($p'_0 = 400$ kPa) tests concentrated on symmetrical two-way conditions (with $q_{mean} = 0$). The procedures mirrored the intact chalk testing by Ahmadi-Naghadeh *et al.* (2022). Target q_{mean} values were applied by undrained strain-controlled loading at a rate of 5% axial strain/day, followed by pauses of 48–72 h in which the specimens sustained their q_{mean} values without drainage until the local axial strain rates fell below 0·005%/day. These steps were critical for distinguishing the specimens' subsequent cyclic straining from any creep provoked by applying the q_{mean} component. Fig. 3 demonstrates how axial strains developed in DCy-D1 to DCy-D4 during their: (*a*) undrained monotonic pre-shearing; (*b*) extended creep pauses; and (*c*) first applied cycle. Also indicated are the corresponding average maximum Young's (E_{max}^{u}) and secant cyclic moduli ($E_{sec}^{u,cyc}$) developed over the first peak-to-trough half cycle. The creep strains are significant and increased with applied q_{mean} to represent a large fraction of the overall straining. The creep pauses allowed the specimens to regain stiffness after pre-shearing and the subsequent cyclic moduli depended primarily on the stress amplitudes imposed. Doughty *et al.* (2018) and Vinck (2021) detail the abrupt stiffness degradation shown by chalk putty specimens; E_{max}^{u} moduli decay by 40% from initial values after shearing to 0·01% axial strain. They ascribe the rapid stiffness degradation to microstructural alteration and brittle re-cementation.

The tests which survived to 10 000 cycles extended for several weeks. All 'surviving' specimens were sheared to undrained monotonic failure; as shown later, stable cycling improved the puttified chalk's monotonic resistance and stiffness.

Undrained cyclic behaviour is often assessed in earthquake geotechnics through testing under symmetrical two-way loading. The failures that define the soils' cyclic resistance ratios (Ishihara, 1996) are defined as occurring when specified double-amplitude (DA) axial (or shear) strain limits are met. Failure under non-symmetrical loading conditions is defined referring to either peak or accumulated cyclic strains (Yang & Sze, 2011). Cyclic failure criteria and strain limits are often tailored to reflect the geo-material's cyclic behaviour and the engineering problems addressed (Wijewickreme & Soysa, 2016).

Noting that stringent deformation tolerances are specified for offshore wind turbine design (Byrne *et al.*, 2017), the cyclic strain limits were set lower than is routine in, for example, liquefaction assessment. Failure was defined by whichever of two criteria was satisfied first

(*a*) criterion A: occurrence of 1% double-amplitude (DA = $\varepsilon_{a,\ peak} - \varepsilon_{a,\ trough}$) axial strain
(*b*) criterion B: absolute peak or trough axial strain ($|\varepsilon_a|$) exceeding 1%.

The criteria reflect chalk putty's potentially marked stiffness degradation under cycling. As demonstrated later, they lead to outcomes that are compatible with other measures of cyclic failure, including trends for pore water pressures, shear strength reductions and damping ratios.

UNDRAINED CYCLIC TEST OUTCOMES

Table 3 summarises key outcomes from the cyclic experiments: the axial strains and ranges of cyclic stiffness ($E_{sec}^{u,cyc}$) and damping ratio (D) experienced up to the number of cycles (N_f) at which failure occurred, or the final cycle for tests that survived 10 000 cycles. Discussion on the mean effective stress drift trends follows later.

Cycling from $p'_0 = 200$ *kPa*

Considering the tests performed from $p'_0 = 200$ kPa, Fig. 4 illustrates how N_f varies with the normalised loading parameters $q_{cyc}/(2S_u)$–$q_{mean}/(2S_u)$ and $q_{cyc}/(p'_0)$–$q_{mean}/(p'_0)$. The three unfailed cases are annotated as '$> N_{max}$' where

Downloaded by [] on [30/05/24]. Published with permission by the ICE under the CC-BY license

Table 3. Strains, pore pressure changes, stiffness and damping ratio variations during cyclic loading, considering changes from the first cycle up to the N_f cycle, or final cycle in the unfailed tests

Test	$q_{mean}/(2S_u)$	$q_{cyc}/(2S_u)$	$q_{max}/(2S_u)$	Imposed cycles, N_{max}	N_f*	ε_a at N_f: %	ε_a/N_f: %	r_u: %†	Secant cyclic $E_{sec}^{u,cyc}$: MPa	Damping ratio, D: %‡
DCy-A1	0	0·30	0·30	10 024	Unfailed	0·078	$7·78 \times 10^{-6}$	0·10→34·5	903→1166	4·80→3·70
DCy-B1	0	0·45	0·45	717	486(A)	−0·210	$-4·32 \times 10^{-4}$	1·91→85·3	951→14·0	6·51→21·2
DCy-C1	0·30	0·30	0·60	10 058	Unfailed	0·085	$8·45 \times 10^{-6}$	32·1→54·1	1067→1155	9·53→8·06
DCy-C2	0·15	0·45	0·60	676	645(B)	0·829	$1·29 \times 10^{-3}$	20·2→95·7	918→9·3	12·8→26·4
DCy-C3	0	0·60	0·60	181	65(A)	−0·023	$-3·54 \times 10^{-4}$	3·86→77·2	841→23·2	13·0→21·3
DCy-CX	−0·15	0·45	−0·60	361	357(A, B)	−0·516	$-1·45 \times 10^{-3}$	10·1→80·3	1067→13·9	4·82→19·9
DCy-D1	0·79	0·17	0·96	9600	Unfailed	0·147	$1·53 \times 10^{-5}$	42·8→67·4	1334→1444	5·56→2·95
DCy-D2	0·57	0·30	0·87	10 614	5528(B)	0·984	$1·78 \times 10^{-4}$	40·1→82·7	1160→269·7	6·90→20·1
DCy-D3	0·44	0·44	0·88	240	183(B)	0·926	$5·06 \times 10^{-3}$	22·2→92·4	1045→35·6	10·9→25·9
DCy-D4	0·28	0·60	0·88	58	47(A, B)	0·523	0·011	30·3→90·2	955→21·6	11·1→25·7
DCy-D5	0	0·75	0·75	170	≈18	−0·005	$-2·78 \times 10^{-4}$	6·45→76·9	508·0→46·9	17·9→23·9
DCy-A1-E	0	0·30	0·30	10 085	Unfailed	0·036	$3·57 \times 10^{-6}$	0·40→64·2	1428→1023	4·51→7·35
DCy-B1-E	0	0·45	0·45	149	142(A)	−0·071	$-5·0 \times 10^{-4}$	1·81→89·0	1236→34·3	8·15→22·1
DCy-C3-E	0	0·60	0·60	57	50(A)	−0·080	$-1·6 \times 10^{-3}$	2·70→82·5	1190→57·3	12·2→24·1
DCy-D5-E	0	0·75	0·75	18	16(A, B)	−0·085	$-5·31 \times 10^{-3}$	6·56→67·3	815·0→80·9	17·0→23·3

*Superscripts (A) and (B) denote the applied cyclic failure criteria. Cycling control of test DCy-D5 deteriorated as specimen softened significantly after 13 cycles.
†r_u, pore water pressure ratio (%), defined as: $r_u = (p'_0 - p')/p'_0 = \Delta u/p'_0$
‡Damping ratio calculated as: $D = A_{loop}/(4\pi A_{elastic})$; A_{loop} – area enclosed by a stress–strain (q–ε_a) loop for a complete sinusoidal stress cycle; $A_{elastic}$ – unloading half-cycle elastic triangle area with height as q_{cyc} (= $(q_{peak} - q_{trough})/2$) and width as cyclic strain (= $(\varepsilon_{peak} - \varepsilon_{trough})/2$).

N_{max} is the number of stress cycles applied. Two nominal $N_f = 1$ contour lines are plotted from (q_{mean}, q_{cyc}) = (0, $2S_u$) to ($2S_u$, 0) and (q_{mean}, q_{cyc}) = (0, $2S_u$) to ($-2S_u$, 0), neglecting minimal variations in S_u between compression and extension (see Fig. 2) and any possible rate dependency of shear strength between monotonic shearing at 5% per day and that developed over the final cycle of loading.

A tentative family of curved N_f (= 10, 30, 100, 300, 1000, 3000 and 10 000) contours that extends to $q_{mean}/(2S_u) = -0·15$ is included to illustrate stress interaction patterns in the one- and two-way cycling regions of the 200 kPa p'_0 tests. Nominal contours are shown as dashed straight lines over the unpopulated extension region and link the contours towards a putative lower $q_{cyc}/(2S_u)$ limit of 0·15. The lower level, high N_f, contours show less curvature and tighter spacings than those representing high-level cycling. The interactive stress diagram region below the $N_f = 10\,000$ contour represents the stable area within which, although strains could accumulate slowly and effective stresses reduce, cyclic failure did not occur.

As shown in Fig. 4, the contours applying in the one-way compressive cyclic region ($q_{mean} \geq q_{cyc}$) situated above the $N_f = 10\,000$ contour, curve downwards rapidly towards the right-hand corner ($q_{cyc}/(2S_u) = 0$). The interpreted two-way contours (where $q_{mean} \leq q_{cyc}$) confirm that chalk putty is more susceptible to compression–extension loading than one-way compression. Similar interactive failure schemes were established from axial cyclic loading field tests on piles driven in chalk by Buckley *et al.* (2018).

The test outcomes for the 400 kPa p'_0 tests are broadly compatible with the contours in Fig. 4, although the higher pressure tests developed excess pore pressures at higher rates and failed at a significantly earlier stage in DCy-B1-E, as detailed later. The chalk's response to high-level cyclic loading is demonstrated by two unstable tests, DCy-C3 and DCy-D4, which were pre-sheared to different q_{mean} but cycled with identical q_{cyc}. Figs 5 and 6 plot their stress–strain response, the overall effective stress paths as well as zoomed-in illustrations of six illustrative cycles prior to and shortly after their nominal failure at $N = N_f$. Fig. 7 shows how the secant undrained cyclic Young's modulus ($E_{sec}^{u,cyc}$) and damping ratio (D) evolved in test DCy-D4, showing the following.

(*a*) Axial strain accumulation accelerates markedly as cyclic failure develops. Straining tended towards a positive ε_a (bulging) pattern in DCy-D4, while negative ε_a (and necking) developed in DCy-C3. While DCy-D4 satisfied failure criteria A and B simultaneously (at $N_f = 47$), DCy-C3 met criterion B one cycle after matching criterion A at $N_f = 65$.

(*b*) Stress–strain curves fall initially in tight bands, fanning out as failure approached. 'Kinks' (as termed by Wijewickreme & Soysa (2016)) were evident in the post-N_f stress–strain loops, where strain hardening occurred and (tangent) stiffnesses increased as deviatoric stresses cycled towards their peaks and troughs.

(*c*) Effective stress paths drift leftward invariably as pore water pressures grow. The paths traversed the PT points and slopes defined by monotonic loading (see Fig. 2), as well as the critical state slopes M.

(*d*) Both contractive and dilative behaviour occurs during individual cycles, as shown in Fig. 6. Best-fit lines drawn through the cyclic PT points identified from the effective stress path loops of two-way cyclic tests with $q_{mean} = 0$ indicate $(q/p')_{PT}^{cyc}$ gradients of ≈ 0·54 and 0·38 in compression and extension, respectively, that fall well below the monotonic PT stress ratios. Mao & Fahey (2003) report similar findings for calcareous silts as do Porcino *et al.* (2008) for an uncemented carbonate sand under cyclic simple shear.

Downloaded by [] on [30/05/24]. Published with permission by the ICE under the CC-BY license

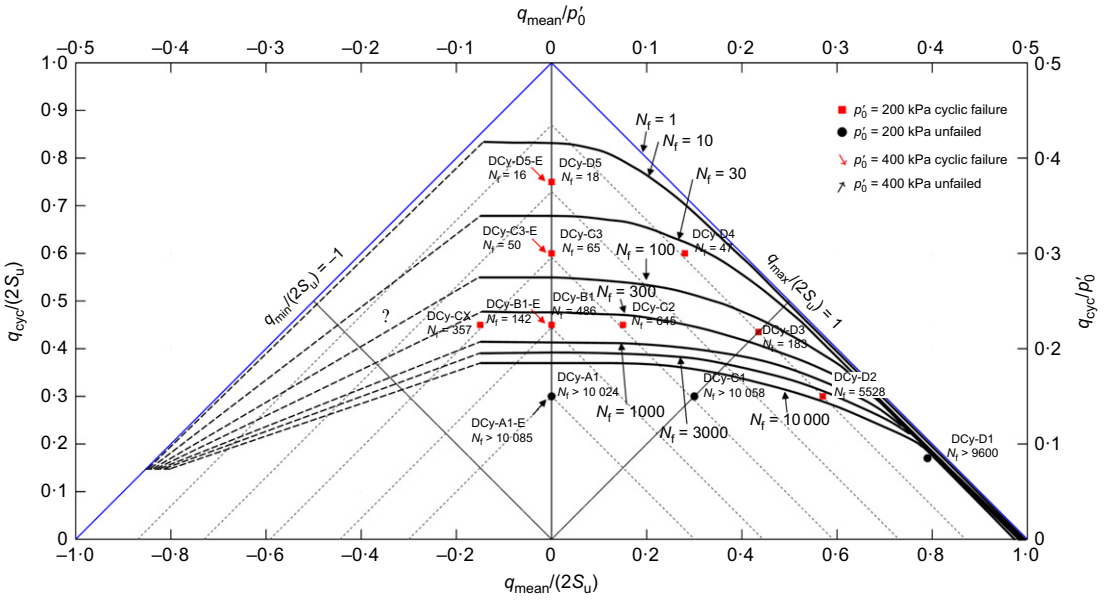


Fig. 4. Cyclic interaction diagram expressed in normalised $q_{cyc}/(2S_u)$–$q_{mean}/(2S_u)$ and q_{cyc}/p'_0–q_{mean}/p'_0 stress space, also indicating the interpreted contours of number of cycles (N_f) to failure for p'_0 = 200 kPa and p'_0 = 400 kPa tests series as summarised in Table 3

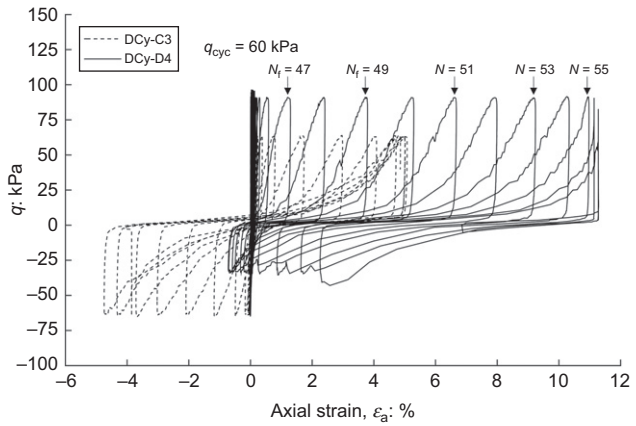


Fig. 5. Unstable cyclic response in tests DCy-C3 and DCy-D4: stress–strain behaviour

(*e*) There is systematic variation in the damping ratio and cyclic stiffness trends. Damping ratios show maxima near failure, followed by marked post-failure reductions as cyclic strains increase. Doygun & Brandes (2020) reported similar, although less abrupt, post-peak decreases for sands.

Equivalent traces are shown in Fig. 8 for two typical 'stable' ($N_f > 10\,000$) tests, DCy-A1 and DCy-D1, with the latter being pre-sheared to the highest q_{mean} and both being cycled with the lowest q_{cyc} in their sub-group. The specimens accumulated only small axial strains over ≈10 000 cycles, developing ε_a–N patterns that can be matched by power-law functions ($\varepsilon_a = a \times N^b$) with $b = 0{\cdot}502$ for both cases. Their stress–strain loops evolved steadily, with moderately increasing cyclic stiffnesses and decreasing damping ratios, as listed in Table 3. Applying a large number of such low-level cycles resulted in a stable, non-linear, but principally reversible response that enhanced the destructured chalk's cyclic resistances. Similar outcomes were reported for silica sands (by Aghakouchak *et al.* (2015)) and stiff glacial till (see Ushev & Jardine (2022)). The pore water pressure ratio r_u ($= (p'_0 - p')/p'_0 = \Delta u/p'_0$, $p'_0 = 200$ kPa) tended to stabilise after ≈2000 cycles and eventually reached 34·5% and 67·4% in DCy-A1 and DCy-D1, respectively. The specimens' cyclic stress path orientations correlated directly with their position relative to the $(q/p')^{cyc}_{PT}$ lines indicated in Fig. 8.

A 'transitional' response, between the above 'stable' and 'unstable' styles, was observed in DCy-D2 under $q_{mean}/(2S_u) = 0{\cdot}57$ and $q_{cyc}/(2S_u) = 0{\cdot}3$. Fig. 9 shows how the specimen's axial strain accumulated almost linearly up to $N = 4000$ and accelerated rapidly up to $N \approx 7000$, followed by a far slower 'near-stable' trend towards $N = 10\,000$, leading to a large ultimate strain of 5·5%. Strain criterion A was met when peak axial strain reached 1% at $N_f = 5528$, while the strain amplitude remained far below the 1% criterion B limit throughout. The specimen's resistance to loading (from q_{min} to q_{max}) was maintained by its tendency to dilate, which kept r_u largely constant at 82% and the effective stress loops settled to a stable pattern after $N > 7000$.

Cycling from p'_0 *= 400 kPa*

Cycling from $p'_0 = 400$ kPa and $p'_0 = 200$ kPa (with $q_{mean} = 0$) provoked broadly compatible cyclic patterns. Although the higher pressure tests developed lower (absolute) strains and higher cyclic stiffness under similar normalised loading levels (see Table 3), higher pore water pressure ratios were observed. The unfailed test DCy-A1-E developed a final r_u twice that of its low-pressure equivalent DCy-A1 after 10 000 cycles, while unstable test DCy-B1-E developed pronouncedly more rapid r_u growth than DCy-B1 (see Fig. 10). Cyclic failure was accompanied by marked and simultaneous changes in axial strains, pore water pressures, cyclic stiffness and damping (see Fig. 7). Fig. 10 also gives further details on how the stress path loops evolved in tests DCy-B1 and DCy-B1-E with reference to the $(q/p')^{cyc}_{PT}$ lines indicated by the two-way cyclic tests. The cyclic PT lines appear largely independent of p'_0 level in both triaxial compression or extension.

Cyclic strain accumulation and stiffness trends

The specimens' (permanent) strain (captured at the end of each full-stress cycle) accumulation, cyclic stiffness

Downloaded by [] on [30/05/24]. Published with permission by the ICE under the CC-BY license

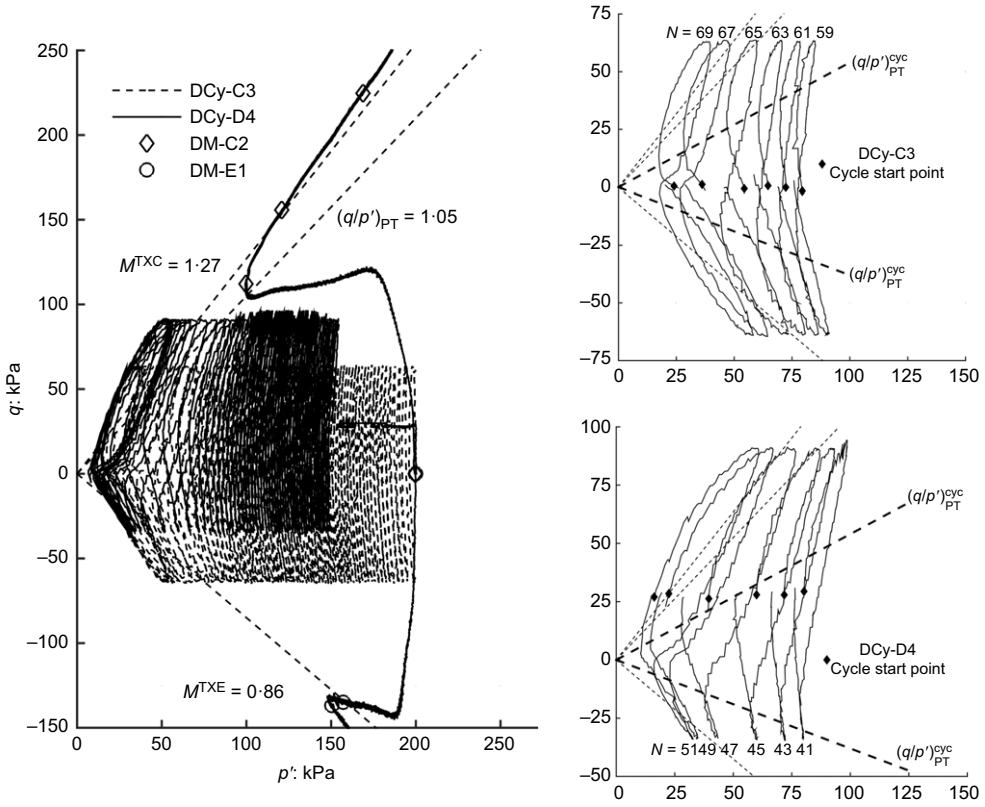


Fig. 6. Stress paths for unstable tests DCy-C3 and DCy-D4 and the identified cyclic PT lines

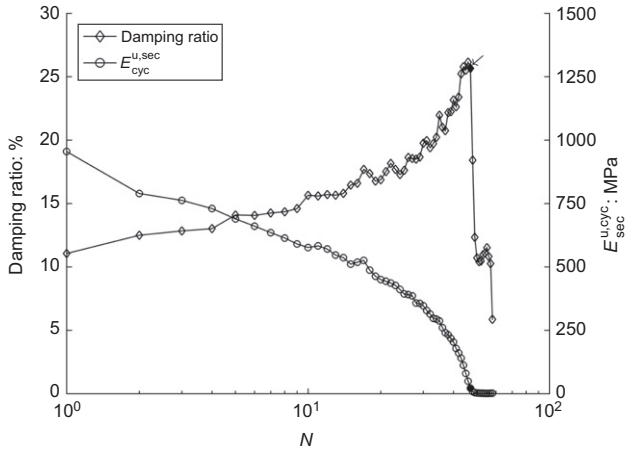


Fig. 7. Damping ratio and cyclic stiffness evolution in unstable test DCy-D4

degradation and mean effective stress drifting patterns can be categorised into three broad groups. Accumulated cyclic strain trends are plotted in Fig. 11(a) for the unstable cyclic resistance ratio 'CRR' ($q_{mean} = 0$) group. The specimens developed minimal ($\leq 0{\cdot}025\%$) straining over their initial stable stages, before trending abruptly towards negative (extension), as cyclic failure approached, and peak-to-trough amplitudes exceeded 1% (criterion A). Most tests developed positive strains over their initial cycles, followed by a trend to reverse towards extension failure. Tests DCy-D5 and DCy-D5-E which cycled with the highest ($q_{cyc}/(2S_u)$) ratio of 0·75 accumulated negative strains throughout. The overall straining patterns were consistent between the $p'_0 = 200$ and

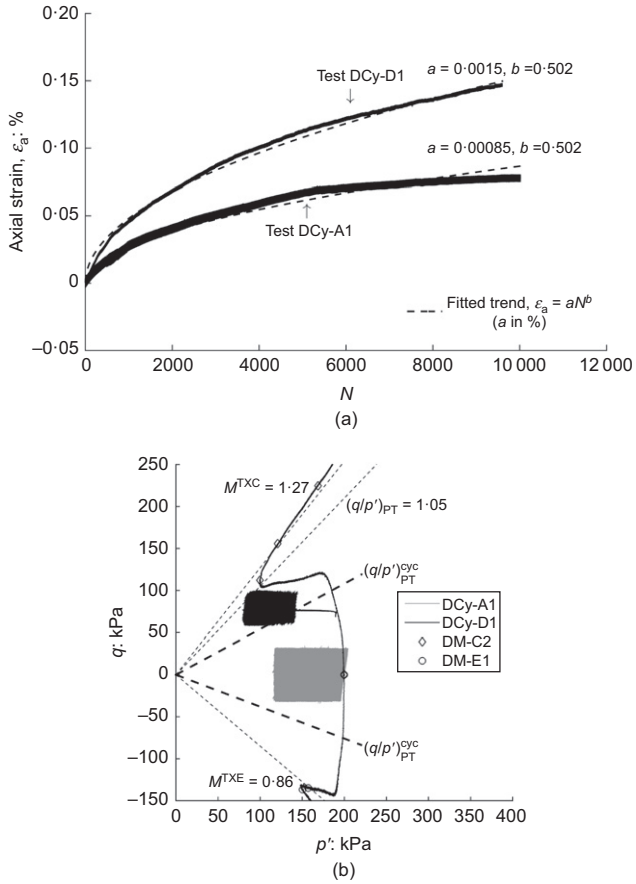


Fig. 8. Unfailed ($N_f > 10\,000$) tests DCy-A1 and DCy-D1: (a) axial strain; (b) effective stress path

Downloaded by [] on [30/05/24]. Published with permission by the ICE under the CC-BY license

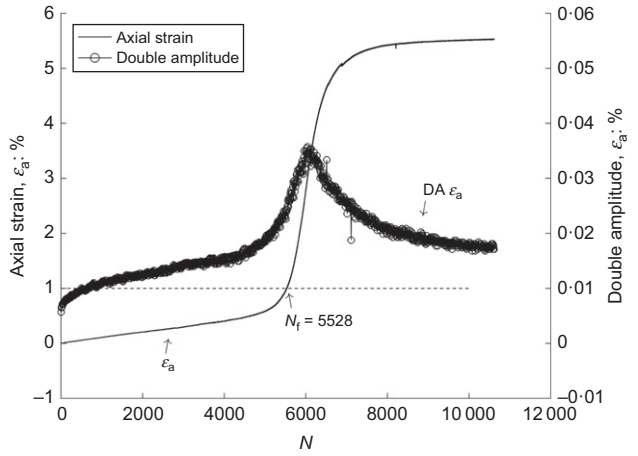


Fig. 9. Axial strain accumulation and double-amplitude trends for the 'transitional' test DCy-D2

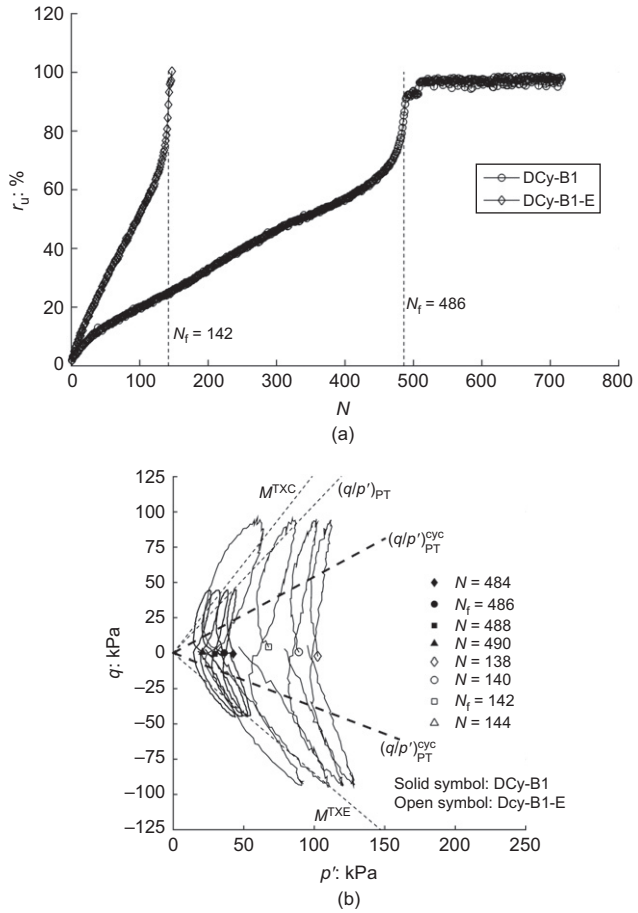


Fig. 10. Tests DCy-B1 (p'_0 = 200 kPa) and DCy-B1-E (p'_0 = 400 kPa): (a) pore water pressure ratio; (b) selected stress path loops near cyclic failure

400 kPa tests, while their cyclic stiffnesses were markedly dependent on the levels of p'_0 and cyclic stress ratio, as shown in Fig. 12.

Figures 11(b) and 12 plot the corresponding trends for the unstable $q_{mean} \neq 0$ group tests. Axial strains accumulated in the direction of pre-shearing q_{mean} and the straining was generally more abrupt in tests with higher $q_{cyc}/(2S_u)$ or negative q_{mean} (test DCy-CX). Test DCy-D2 developed 'transitional' cycling behaviour (as discussed previously) with its stiffness degrading significantly over its initial 6000 cycles

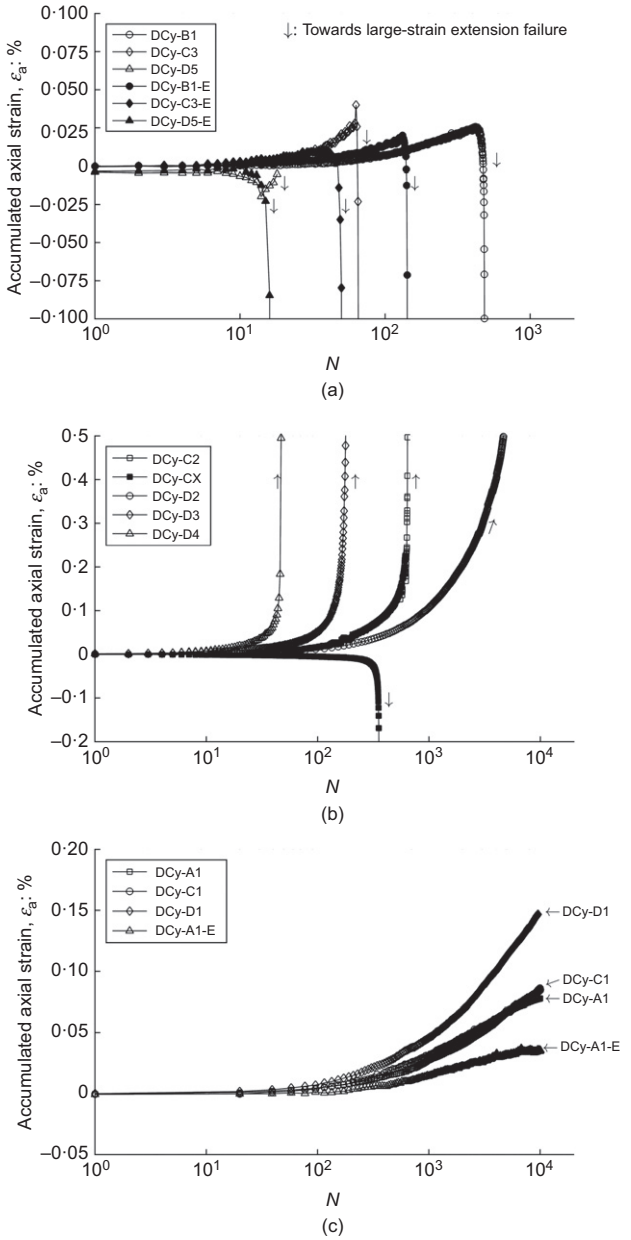


Fig. 11. Trends for accumulated cyclic strain against number of cycles: (a) unstable group, q_{mean} = 0; (b) unstable group, $q_{mean} \neq 0$; (c) 'stable' (unfailed within 10 000 cycles) group

but recovering subsequently. As revealed in Fig. 7, damping ratios generally increased over the initial cycles with the applied $q_{cyc}/(2S_u)$ ratio, but reached similar peaks (on average 23·4%, see Table 3) as failure approached.

Specimens in the unfailed group ($N_f > 10\,000$) accumulated moderate (< 0·16%) permanent strains, as demonstrated in Fig. 11(c). The cyclic stiffness decreased slightly but gained ultimately by on average 15% in the p'_0 = 200 kPa tests, as listed in Table 3, while the elevated stress test (DCy-A1-E) lost 30% stiffness, correlating with its much greater proportional reduction in p' (see Fig. 14(a) later).

Figure 8 gives examples of how equation (1) power-law functions match the evolution of permanent cyclic strains with N. A similar approach was applied to other unfailed tests, and to the initial stages of unstable tests prior to strain reversal or significant acceleration. Parameters a and b were controlled predominantly by q_{cyc} and were relatively insensitive to q_{mean}. The empirical curve-fitting equations (2) and (3) provide a means of estimating permanent strains

Downloaded by [] on [30/05/24]. Published with permission by the ICE under the CC-BY license

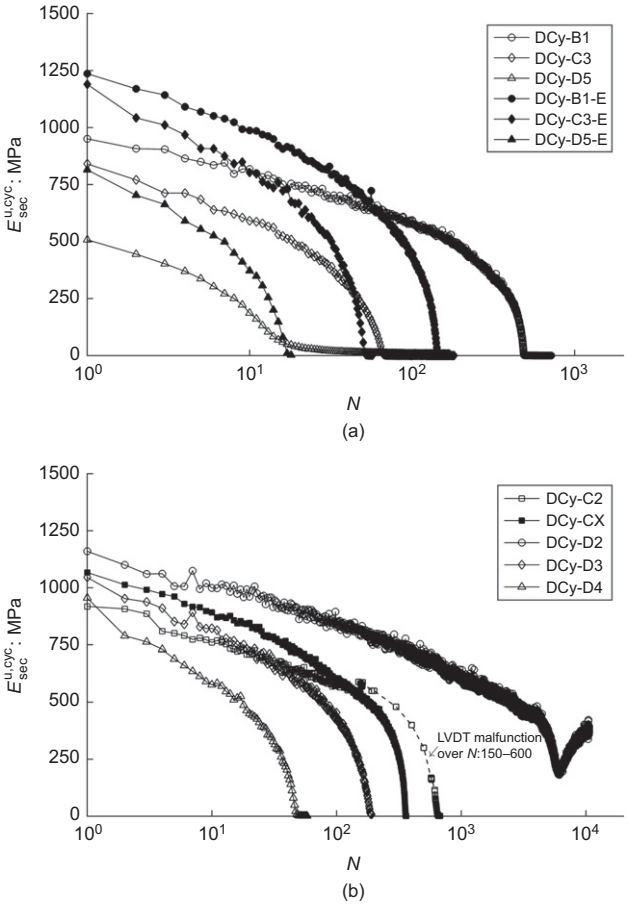


Fig. 12. Cyclic stiffness degradation trends for unstable tests: (a) $q_{mean} = 0$; (b) $q_{mean} \neq 0$

developed prior to cyclic failure and can be employed when developing and calibrating analyses of overall pile response to axial cycling through global or local t–z approaches, as described by Jardine (2020).

$$\varepsilon_a = a \times (N)^b \tag{1}$$

$$a = -0{\cdot}0011 \times \ln\left[\frac{q_{cyc}}{p'_0}\right] - 0{\cdot}0012(\text{in }\%) \tag{2}$$

$$b = 0{\cdot}265 \times e^{[5{\cdot}328 \times (q_{cyc}/p'_0)]} \tag{3}$$

Cyclic resistance ratios

Drawing on the symmetrical cycling tests (with $q_{mean} = 0$), Fig. 13 demonstrates trends for cyclic stress ($q_{cyc}/(2S_u)$) and resistance (CRR: $q_{cyc}/(2p'_0)$) ratios against N_f or N_{max}. The trends are compatible with those commonly observed for carbonate sands and silts (Sanin & Wijewickreme, 2006; Porcino *et al.*, 2008) and can be matched by the function given as equation (4), which is plotted as a dashed line in Fig. 13 through both the $p'_0 = 200$ and 400 kPa test points.

$$\frac{q_{cyc}}{(2S_u)} = 0{\cdot}24 + \frac{1}{1{\cdot}32 + 0{\cdot}35 \times [\log_{10}(N_f)]^{2{\cdot}5}} \tag{4}$$

The $q_{cyc}/(2p'_0)$–N_f trend can be derived by noting the correlation of $2S_u \approx$ triaxial compression $(q)_{PT} \approx p'_0/2$ found in the monotonic tests. The function implies a $q_{cyc}/(2S_u)$ ratio of 0·32 at $N_f = 10\,000$ and a lower limit of 0·24 below which regular symmetric two-way loading can be applied

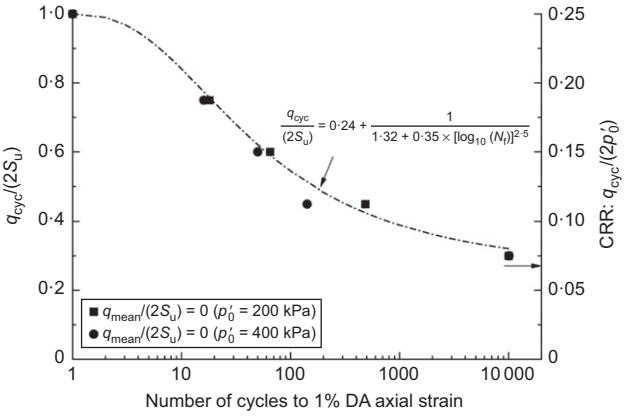


Fig. 13. Trends for cyclic stress ratio ($q_{cyc}/(2S_u)$) and cyclic resistance ratio (CRR: $q_{cyc}/(2p'_0)$) against number of cycles to failure (N_f)

indefinitely. The $q_{cyc}/(2S_u)$ limit of 0·24 is lower than in tests DCy-A1 and DCy-A1-E, which did not show fully stable trends for mean effective stress (discussed below). The lower limit exceeds the linear elastic (Y_1) threshold with $\Delta q/(2S_u) \approx 0{\cdot}22$ developed under monotonic loading (as discussed previously) and could be regarded as the limit to the outer kinematic Y_2 surface within which specimens develop hysteretic closed stress–strain loops with non-linear yet recoverable straining (Smith *et al.*, 1992; Kuwano & Jardine, 2007; Ushev & Jardine, 2022).

MEAN EFFECTIVE STRESS DRIFTS

The tests' detailed, cycle-by-cycle measurements enable further interpretation and application in the laboratory test-based predictive framework for axial cyclic pile loading assessment described by Jardine *et al.* (2012), Rattley *et al.* (2017) and Jardine (2020). Figs 14(a)–14(c) plot the ratios of mean effective stress changes ($\Delta p' = p'_{N=i} - p'_{N=1}$) for all tests by reference to specimens' pre-shearing p'_0 of 200 or 400 kPa, in ascending q_{cyc}/p'_0 sequences. The following observations apply.

(*a*) All tests showed $\Delta p'/p'_0$ decreasing continuously against N. It is possible that cycling at lower levels would identify conditions under which no reduction occurred.
(*b*) Steeper rates of $\Delta p'/p'_0$ drift were observed in specimens cycled from higher pressures ($p'_0 = 400$ kPa) under q_{cyc}/p'_0 ratios $< 0{\cdot}3$ than in equivalent $p'_0 = 200$ kPa experiments, but the influence became less discernible at higher q_{cyc}/p'_0.
(*c*) The rates of $\Delta p'/p'_0$ degradation depended principally on the cyclic stress ratio (q_{cyc}/p'_0). The influence of q_{mean}/p'_0 was modest over the central portion of the interactive stress diagram and became more significant as $(q_{cyc} + q_{mean})/p'_0$ exceeded 0·4 in the $p'_0 = 200$ kPa tests, causing the N_f contours to curve down markedly (see Fig. 4).

Tests on dense sands and stiff clays show that pre-cycling with relatively high stress ratios (as occurs during pile driving) reduces and, at low q_{cyc}/p'_0 can even reverse, the $\Delta p'/p'_0$ drift rates observed on renewed cycling at lower q_{cyc}/p'_0 levels (Aghakouchak, 2015; Aghakouchak *et al.*, 2015; Rattley *et al.*, 2017). It remains to be established whether such trends apply to destructured chalk. The above authors demonstrated how the $\Delta p'/p'_0$–N (or $\Delta\sigma'_z/\sigma'_{z0}$–$N$) relationships from cyclic triaxial, hollow cylinder apparatus or simple shear tests could be expressed by the power-law form in

Downloaded by [] on [30/05/24]. Published with permission by the ICE under the CC-BY license

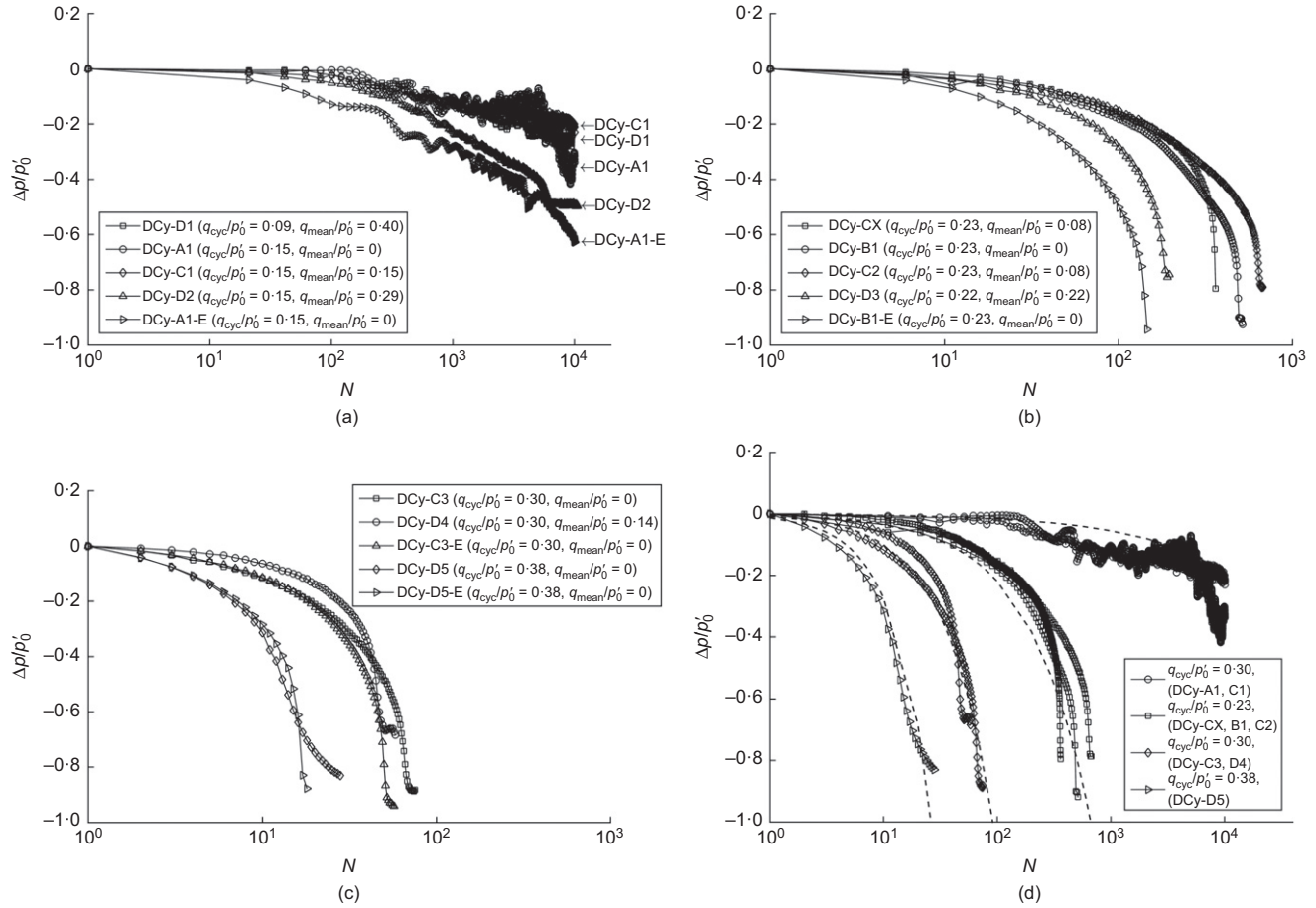


Fig. 14. Drifting trends for mean effective stress during cycling: (a) $q_{cyc}/p'_0 \leq 0{\cdot}15$; (b) $q_{cyc}/p'_0 \approx 0{\cdot}23$; (c) $q_{cyc}/p'_0 \geq 0{\cdot}30$; (d) fitted trends for tests with $p'_0 = 200$ kPa and mostly $(q_{cyc} + q_{mean})/p'_0 < 0{\cdot}4$

equation (5) and applied to generate shaft capacity degradation trends that match trends from cyclic pile tests (Jardine & Standing, 2012).

$$\frac{\Delta p'}{p'_0} = A \times \left[B + (q_{cyc}/p'_0)\right] \times N^C \tag{5}$$

where A, B and C are parameters defining the rate of p' degradation and the maximum cyclic stress ratio that could lead to beneficial, null, or deleterious cycling effects. The $p'_0 = 200$ kPa tests with $(q_{cyc} + q_{mean})/p'_0 < 0{\cdot}4$ indicate $A = -0{\cdot}05$ and $B = -0{\cdot}12$, regardless of the applied q_{cyc}/p'_0 ratio, with the following best-fitting linear correlation for parameter C.

$$C = 3{\cdot}48 \times \frac{q_{cyc}}{p'_0} \tag{6}$$

The chalk putty tests indicated a far wider $0{\cdot}3 < C < 1{\cdot}3$ range than reported for dense sands or stiff clays. Fig. 14(d) demonstrates how the above correlations and parameters provide generally good matches (shown as dashed lines) with the (mainly $p'_0 = 200$ kPa) experiments. Note that fully stable responses are expected when $q_{cyc}/p'_0 < |B| = 0{\cdot}12$ (or $q_{cyc}/(2S_u) = 0{\cdot}24$), in keeping with the $q_{cyc}/(2S_u)$ lower limit implicit in equation (4).

POST-CYCLIC MONOTONIC SHEAR AND CRITICAL STATE BEHAVIOUR

Table 4 summarises key outcomes of post-cyclic monotonic undrained shearing stages conducted after the five tests that sustained 10 000 cycles, listing the initial stress conditions and pore pressure ratios (r_u) along with the initial maximum and normalised Young's moduli (E^u_{max}) and the ultimate stresses and strains attained. When sheared monotonically from initial conditions with an average $r_u = 62\%$, the pre-cycled specimens exhibited maximum Young's moduli that were broadly comparable to those of 'virgin' specimens sheared from $r_u = 0$ (see Table 1). More pronounced changes were found in the putty's normalised stiffness ratios, $(E^u_{max}/p_{ref})/(p'_0/p_{ref})^{0{\cdot}5}$, where $p_{ref} = 101{\cdot}3$ kPa, which were on average 58% higher than for the monotonic tests conducted without pre-cycling. Long-term (≈ 35 days) undrained low-amplitude stress cycling enhanced stiffness and led to slightly higher shear strengths. The pre-cycled specimens manifested principally dilative responses and trended towards ultimate shear strengths with ultimate stress ratios $M = (q/p')_{ult}$ rising moderately from 1·27 to 1·34.

Figure 15 considers the state paths followed in the v–$\log(p')$ plane by the destructured chalk during undrained triaxial compression tests from p'_0 of 70, 200 and 400 kPa. This treatment enables further interpretation and modelling of chalk's mechanical response and destructuration behaviour with critical-based approaches, such as the Lagioia & Nova (1995) framework.

As noted earlier, the pre-shearing states achieved by the destructured specimens after their initial 'in-mould' and later isotropic consolidation and creep stages fell (unexpectedly) well below the CRS 1D compression path, when projected assuming $K_0 = 1 - \sin(\phi'_{cs}) = 0{\cdot}48$ from Fig. 1. The tests' PT points are shown and a critical state relationship is drawn through the tests' ultimate shearing points, which fall, as

Downloaded by [] on [30/05/24]. Published with permission by the ICE under the CC-BY license

Table 4. Summary of maximum undrained Young's moduli (E^{u}_{max}), pore water pressure ratio, ultimate stress states and the corresponding axial strains (in brackets) of the post-cyclic monotonic tests

Test	p': kPa	q: kPa	r_{u0}: %	E^{u}_{max}: MPa	$\left(\frac{E^{u}_{max}}{p_{ref}}\right)/\left(\frac{p'_0}{p_{ref}}\right)^{0.5}$*	$q_{(ult)}$: kPa (ε_a: %)	$p'_{(ult)}$: kPa	$(q/p')_{ult}$	ϕ'_{ult}: degrees
DCy-A1	120·2	0	39·9	1265·8	11 471	837·1 (31·5%)	640·4	1·31	33·2
DCy-C1	103·6	30	52·7	1159·4	11 319	1002 (27·8%)	744·9	1·35	
DCy-D1	94·8	77·3	65·3	1110·4	11 330	919·5 (22·3%)	705·3	1·30	
DCy-D2	47·6	67·2	87·4	936·0	13 483	645·2 (19·5%)	465·9	1·38	
DCy-A1-E	143·4	0	64·2	1492·4	12 384	1205·3 (18·8%)	881·0	1·37	

*p_{ref}, reference pressure (101·3 kPa).

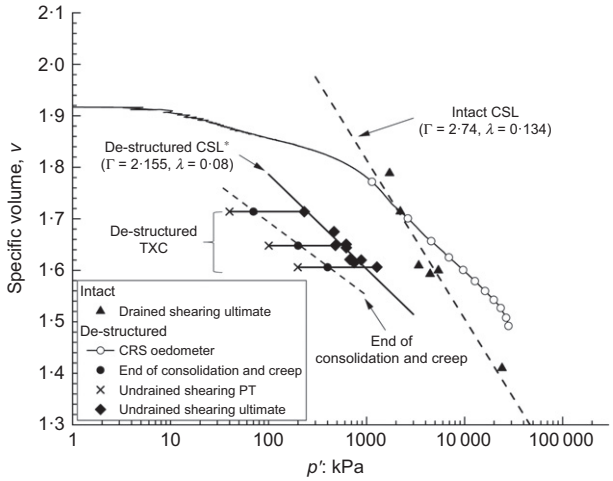


Fig. 15. Critical state relationships established for destructured and intact chalk

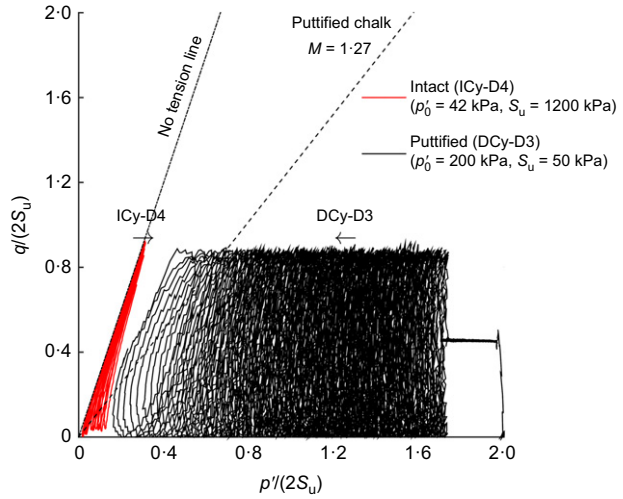


Fig. 16. Effective stress path of intact (Ahmadi-Naghadeh *et al.*, 2022) and destructured chalk (samples with $q_{cyc}/(2S_u) = q_{mean}/(2S_u) \approx 0{\cdot}44$; plotted up to $N_f + 3$ cycles)

expected, below the 1D compression curve, but also below the critical state relationship established for intact chalk through high-pressure triaxial tests. It is interesting to speculate whether the intact and destructured critical state line (CSL) relationships would fall closer if it had been possible to compress beyond the ≈30% maximum axial strain that can be imposed in triaxial tests.

The destructured samples' tendency to dilate significantly post-PT is compatible with their 'dry' position relative to their CSL. In terms of the Been & Jefferies (1985) framework, the specimen's state parameters ($\psi = e - e_{cs}$) decrease systematically as p'_0 grows, a trend that is reflected in the high-pressure tests' tendency to produce higher cyclic excess pore pressures.

COMPARISON OF INTACT AND DESTRUCTURED CHALK

As noted in the introduction, the cyclic response of piles driven in chalk is affected by both the putty zone around the shaft and the surrounding intact mass. It is therefore interesting to contrast the undrained cyclic triaxial behaviour of chalk in both conditions, drawing on representative paired tests that applied identical mean and cyclic stresses. Fig. 16 offers such a comparison for tests with $q_{cyc}/(2S_u) = q_{mean}/(2S_u) \approx 0{\cdot}44$. Cyclic failure in the putty involves pore pressure build-up, leftward drifting of the effective stress path, cyclic stiffness loss and growing damping ratios (see also Figs 5–7 and 10–12). In contrast, the intact chalk shows a very stiff cyclic response, with little or no sign of pore pressure change or impending instability. The cyclic effective stress paths remain within a tight band beforehand and until shortly before abrupt brittle failure, which leads to markedly dilative pore pressure trends. Ahmadi-Naghadeh *et al.* (2022) conclude that the intact response is closer to that of harder rocks and solids, such as concretes and metals, whose cyclic or fatigue failure is dominated by their inherent microstructures and triggered by local stress concentrations that promote progressive wear and shearing.

SUMMARY AND CONCLUSIONS

Heavily destructured soft putty forms in the field under intense compression or large-strain, repetitive shearing. Understanding the putty's behaviour after reconsolidation is crucial to advancing driven pile design in chalk. This paper reports 20 high-resolution triaxial experiments and other tests on putty formed by dynamic compaction followed by re-consolidation and explores their responses to both monotonic and one- and two-way sinusoidal deviatoric undrained loading. The experiments, which ran in parallel alongside an intact chalk programme, led to the following main conclusions.

(*a*) Chalk that is destructured by dynamic compaction manifests distinctly time-dependent behaviour. Incorporating maintained-stress creep stages is essential to distinguishing the separate impacts of initial monotonic shearing from subsequent cyclic loading.

(*b*) Chalk putty's response to undrained monotonic loading resembles that of silts and silty sands,

Downloaded by [] on [30/05/24]. Published with permission by the ICE under the CC-BY license

developing well-defined PT and critical states over medium to large strains.

(*c*) Reconsolidated putty's response to undrained high-level cyclic loading involves both contractant and dilative stages, with an overall trend for positive pore pressure build-up, leftward effective stress path drift, permanent strain accumulation, gradual cyclic stiffness losses and increasing damping ratios.

(*d*) Experiments on isotropically consolidated samples identify cyclic PT that occurs at lower q/p' ratios than under monotonic loading and appears largely independent of p'_0 level, mean and cyclic stress ratio, as well as loading direction. The cyclic stress paths were not bounded by the critical state stress ratios identified from monotonic tests.

(*e*) The maximum number of cycles that the reconsolidated putty can sustain under given normalised mean and cyclic stresses can be expressed in interactive stress diagrams that delineate the stress conditions under which cyclic loading leads to either failure in given numbers of cycles or causes no deleterious effect. Puttified chalk is particularly susceptible to high-level two-way loading that involves stress reversals between compression and extension.

(*f*) Empirical correlations provide predictions for the number of cycles to failure (N_f) when cycling at fixed cyclic stress ratios ($q_{cyc}/(2S_u)$) under the most critical $q_{mean} = 0$ two-way loading conditions.

(*g*) Samples consolidated to different pressure levels manifest broadly similar overall cyclic loading responses, although raising the pressures increases the reconsolidated putty's susceptibility to cyclic loading of lower amplitude.

(*h*) Degradation trends for mean effective stress ($\Delta p'/p'_0$–N) were found to be affected most strongly by cyclic stress ratio and well correlated by power laws. The calibrated $\Delta p'/p'_0$–N correlation provides important inputs for laboratory-based global cyclic stability analysis of axially loaded driven piles in chalk.

(*i*) Application of large numbers of low-level cycles invokes a principally reversible, although non-linear, response. Specimens that survive long-term undrained cycling offer greater post-cyclic stiffness and shear strength than 'virgin' specimens.

(*j*) The re-consolidated putty's response to undrained monotonic and cyclic loading differs markedly from that of intact chalk. The putty responds as a fine granular material, whereas the intact chalk manifests fatigue failure mechanisms that resemble those of harder rocks and solid materials.

Overall, the interactive cyclic triaxial stress diagrams, effective stress drift, permanent displacement and stiffness trends provide key information to aid both the interpretation of the ALPACA field tests and the cyclic design of piles driven in other comparable chalks.

ACKNOWLEDGEMENTS

The experimental study was undertaken as part of the ALPACA and ALPACA Plus Projects funded by the Engineering and Physical Science Research Council (EPSRC) grant EP/P033091/1, Royal Society Newton Advanced Fellowship NA160438 and Supergen ORE Hub 2018 (EPSRC EP/S000747/1). Byrne is supported by the Royal Academy of Engineering under the Research Chairs and Senior Research Fellowships scheme. The authors acknowledge the provision of additional financial and technical support by steering committee members and partners: Atkins, Cathie Associates, Equinor, Fugro, Geotechnical Consulting Group (GCG), Iberdrola, Innogy, LEMS, Ørsted, Parkwind, Siemens, TATA Steel and Vattenfall. Imperial College EPSRC Centre for Doctoral Training (CDT) in Sustainable Civil Engineering and the DEME Group (Belgium) are acknowledged for supporting the doctoral study of Ken Vinck. Invaluable technical support was provided by Steve Ackerley, Graham Keefe, Prash Hirani, Stef Karapanagiotidis at the Department of Civil and Environmental Engineering of Imperial College London is acknowledged gratefully.

NOTATION

A, B, C	fitting parameters for mean effective stress degradation
$A_{elastic}$	unloading half-cycle elastic triangle area with height as q_{cyc}($= (q_{peak} - q_{trough})/2$) and width as cyclic strain ($= (\varepsilon_{peak} - \varepsilon_{trough})/2$)
A_{loop}	area enclosed by a stress–strain (q–ε_a) loop for a complete sinusoidal stress cycle
a, b	fitting parameters for permanent cyclic strain
C_c	compression index of intact specimen
C_c^*	compression index of reconstituted specimen
C_s	swelling index of intact specimen
$C_{\alpha e}$	rate of secondary compression of intact specimen
c'	soil cohesion
D	damping ratio ($= A_{loop}/(4\pi A_{elastic})$)
D_{50}	mean particle diameter
E^u_{max}	maximum undrained Young's modulus
E^u_{sec}	undrained secant vertical Young's modulus
$E^{u,cyc}_{sec}$	cyclic undrained secant vertical Young's modulus
e_0	specimen initial void ratio
G_s	specific gravity
K_0	earth pressure coefficient at rest
M	critical state q/p' stress ratio
N	number of cycles
N_f	number of cycles to failure
p'	mean effective stress
p'_0	initial mean effective stress
q	deviatoric stress
q_{cyc}	cyclic deviatoric stress amplitude ($= (q_{peak} - q_{trough})/2$)
q_f	deviatoric stress at failure
q_{max}	maximum q applied in stress cycle ($= q_{mean} + q_{cyc}$)
q_{mean}	mean q applied in stress cycle
q_{PT}	deviatoric stress at the phase transformation state
q_{peak}	peak q applied in stress cycle ($= q_{max}$)
q_{trough}	minimum q applied in stress cycle ($= q_{mean} - q_{cyc}$)
r_u	pore water pressure ratio ($= (p'_0 - p')/p'_0 = \Delta u/p'_0$)
S_r	saturation degree
S_u	undrained shear strength
Δu	excess pore water pressure
ε_a	axial (vertical) strain
ε_{peak}	axial strain at q_{peak}
ε_r	radial (horizontal) strain
ε_s	shear strain ($= \varepsilon_a$ for undrained triaxial condition)
ε_{trough}	axial strain at q_{trough}
ϕ'_{cs}	critical state shear resistance angle
ϕ'_{peak}	shear resistance angle at peak

REFERENCES

Aghakouchak, A. (2015). *Advanced laboratory studies to explore the axial cyclic behaviour of driven piles*. PhD thesis, Imperial College, London, UK.

Aghakouchak, A., Sim, W. W. & Jardine, R. J. (2015). Stress-path laboratory tests to characterise the cyclic behaviour of piles driven in sands. *Soils Found.* **55**, No. 5, 917–928.

Ahmadi-Naghadeh, R., Liu, T., Vinck, K., Jardine, R. J., Kontoe, S., Byrne, B. W. & McAdam, R. A. (2022). A

Downloaded by [] on [30/05/24]. Published with permission by the ICE under the CC-BY license

laboratory characterization of the response of intact chalk to cyclic loading. *Géotechnique*, https://doi.org/10.1680/jgeot.21.00198.

Alvarez-Borges, F. J., Madhusudhan, B. N. & Richards, D. J. (2018). The 1D normal compression line and structure permitted space of low-medium density chalk. *Géotechnique Lett.* **8**, No. 4, 1–20, https://doi.org/10.1680/jgele.18.00091.

Alvarez-Borges, F., Madhusudhan, B. N. & Richards, D. (2020). Mechanical behaviour of low-medium density destructured white chalk. *Géotechnique Letters* **10**, No. 2, 360–366, https://doi.org/10.1680/jgele.20.00009.

Been, K. & Jefferies, M. G. (1985). A state parameter for sands. *Géotechnique* **35**, No. 2, 99–112, https://doi.org/10.1680/geot.1985.35.2.99.

Bialowas, G. A., Diambra, A. & Nash, D. F. T. (2018). Stress and time-dependent properties of crushed chalk. *Proc. Instn Civ. Engrs – Geotech. Engng* **171**, No. 6, 530–544, https://doi.org/10.1680/jgeen.17.00168.

Buckley, R. M., Jardine, R. J., Kontoe, S., Parker, D. & Schroeder, F. C. (2018). Ageing and cyclic behaviour of axially loaded piles driven in chalk. *Géotechnique* **68**, No. 2, 146–161, https://doi.org/10.1680/jgeot.17.P.012.

Buckley, R. M., Kontoe, S., Jardine, R. J., Barbosa, P. & Schroeder, F. C. (2020a). Pile driveability in low-to-medium density chalk. *Can. Geotech. J.* **58**, No. 5, 650–665, https://doi.org/10.1139/cgj-2019-0703.

Buckley, R. M., Jardine, R. J., Byrne, B. W., Kontoe, S., McAdam, R. A., Ahmadi-Naghadeh, R., Liu, T., Schranz, F. & Vinck, K. (2020b). Pile behavior in low-medium density chalk: preliminary results from the ALPACA project. In *Proceedings of the fourth international symposium on frontiers in offshore geotechnics (ISFOG)* (ed. Z. Westgate). Hawthorne, NJ, USA: Deep Foundation Institute.

Burland, J. B. (1990). On the compressibility and shear strength of natural clays. *Géotechnique* **40**, No. 3, 329–378, https://doi.org/10.1680/geot.1990.40.3.329.

Byrne, B., McAdam, R., Burd, H., Houlsby, G., Martin, C., Beuckelaers, W., Zdravkovic, L., Taborda, D., Potts, D., Jardine, R., Ushev, E., Liu, T., Abadias, D., Gavin, K., Igoe, D., Doherty, P., Gretlund, J. S., Andrade, M. P., Wood, A. M., Schroeder, F., Turner, S. & Plummer, M. (2017). PISA: new design methods for offshore wind turbine monopiles. In *Offshore site investigation and geotechnics – smarter solutions for offshore developments*, vol. 1, pp. 142–161. London, UK: Society for Underwater Technology.

Carotenuto, P., Meyer, V., Strøm, P. J., Cabarkapa, Z., St. John, H. & Jardine, R. J. (2018). Installation and axial capacity of the Sheringham shoal offshore wind farm monopiles – a case history. In *Engineering in chalk: proceedings of the chalk 2018 conference* (eds J. A. Lawrence, M. Preene, U. L. Lawrence and R. M. Buckley), pp. 117–122. London, UK: ICE Publishing.

Carraro, J. A. H., Bandini, P. & Salgado, R. (2003). Liquefaction resistance of clean and nonplastic silty sands based on cone penetration resistance. *J. Geotech. Geoenviron. Engng* **129**, No. 11, 965–976.

Carrington, T. M., Li, G. & Rattley, M. J. (2011). A new assessment of ultimate unit friction for driven piles in low to medium density chalk. In *Proceedings of the 15th European conference on soil mechanics and geotechnical engineering: geotechnics of hard soils – weak rocks* (eds A. Anagnostopoulos, M. Pachakis and C. Tsatsanifos), Part 4, pp. 825–830. Amsterdam, the Netherlands: IOS Press.

Diambra, A., Ciavaglia, F., Harman, A., Dimelow, C., Carey, J. & Nash, D. F. T. (2014). Performance of cyclic cone penetration tests in chalk. *Géotechnique Lett.* **4**, No. 3, 230–237, https://doi.org/10.1680/geolett.14.00050.

Doughty, L. J., Buckley, R. M. & Jardine, R. J. (2018). Investigating the effect of ageing on the behaviour of chalk putty. In *Engineering in chalk: proceedings of the chalk 2018 conference* (eds J. A. Lawrence, M. Preene, U. L. Lawrence and R. M. Buckley), pp. 695–701. London, UK: ICE Publishing.

Doygun, O. & Brandes, H. G. (2020). High strain damping for sands from load-controlled cyclic tests: correlation between stored strain energy and pore water pressure. *Soil Dyn. Earthq. Engng* **134**, 106134.

Hyde, A. F., Higuchi, T. & Yasuhara, K. (2006). Liquefaction, cyclic mobility, and failure of silt. *J. Geotech. Geoenviron. Engng* **132**, No. 6, 716–735.

Ishihara, K. (1996). *Soil behaviour in earthquake geotechnics*. Oxford, UK: Oxford University Press.

Jardine, R. J. (2020). Geotechnics, energy and climate change: the 56th Rankine lecture. *Géotechnique* **70**, No. 1, 3–59, https://doi.org/10.1680/jgeot.18.RL.001.

Jardine, R. J. & Standing, J. R. (2012). Field axial cyclic loading experiments on piles driven in sand. *Soils Found.* **52**, No. 4, 723–736.

Jardine, R. J., Puech, A. & Andersen, K. H. (2012). Cyclic loading of offshore piles: potential effects and practical design. In *Offshore site investigation and geotechnics: integrated technologies – present and future*, pp. 59–97. London, UK: Society of Underwater Technology.

Kuwano, R. & Jardine, R. (2007). A triaxial investigation of kinematic yielding in sand. *Géotechnique* **57**, No. 7, 563–579, https://doi.org/10.1680/geot.2007.57.7.563.

Lagioia, R. & Nova, R. (1995). An experimental and theoretical study of the behaviour of a calcarenite in triaxial compression. *Géotechnique* **45**, No. 4, 633–648, https://doi.org/10.1680/geot.1995.45.4.633.

Mao, X. & Fahey, M. (2003). Behaviour of calcareous soils in undrained cyclic simple shear. *Géotechnique* **53**, No. 8, 715–727, https://doi.org/10.1680/geot.2003.53.8.715.

Mesri, G. & Vardhanabhuti, B. (2006). Discussion of 'secondary compression'. *J. Geotech. Geoenviron. Engng* **132**, No. 6, 817–818.

Porcino, D., Caridi, G. & Ghionna, V. N. (2008). Undrained monotonic and cyclic simple shear behaviour of carbonate sand. *Géotechnique* **58**, No. 8, 635–644, https://doi.org/10.1680/geot.2007.00036.

Rattley, M. J., Costa, L., Jardine, R. J. & Cleverly, W. (2017). Laboratory test predictions of the cyclic axial resistance of a pile driven in North Sea soils. In *Offshore site investigation and geotechnics – smarter solutions for offshore developments*, vol. 2, pp. 636–643. London, UK: Society for Underwater Technology.

Sağlam, S. & Bakır, B. S. (2014). Cyclic response of saturated silts. *Soil Dyn. Earthq. Engng* **61–62**, 164–175.

Sanin, M. V. & Wijewickreme, D. (2006). Cyclic shear response of channel-fill Fraser River Delta silt. *Soil Dyn. Earthq. Engng* **26**, No. 9, 854–869.

Smith, P. R., Jardine, R. J. & Hight, D. W. (1992). The yielding of Bothkennar clay. *Géotechnique* **42**, No. 2, 257–274, https://doi.org/10.1680/geot.1992.42.2.257.

Ushev, E. R. & Jardine, R. J. (2022). The behaviour of Bolders Bank glacial till under undrained cyclic loading. *Géotechnique* **72**, No. 1, 1–19, https://doi.org/10.1680/jgeot.18.P.236.

Vinck, K. (2021). *Advanced geotechnical characterisation to support driven pile design at chalk sites*. PhD thesis, Imperial College, London, UK.

Vinck, K., Liu, T., Jardine, R. J., Kontoe, S., Ahmadi-Naghadeh, R., Buckley, R. M., Byrne, B. W., Lawrence, J., Mcadam, R. A. & Schranz, F. (2022). Advanced in situ and laboratory characterisation of the ALPACA chalk research site. *Géotechnique*, https://doi.org/10.1680/jgeot.21.00197.

Wei, X. & Yang, J. (2019). Characterizing the effects of fines on the liquefaction resistance of silty sands. *Soils Found.* **59**, No. 6, 1800–1812.

Wijewickreme, D. & Soysa, A. (2016). A stress–strain pattern based criterion to assess cyclic shear resistance of soil from laboratory element tests. *Can. Geotech. J.* **53**, No. 9, 1460–1473.

Yang, J. & Sze, H. (2011). Cyclic behaviour and resistance of saturated sand under non-symmetrical loading conditions. *Géotechnique* **61**, No. 1, 59–73, https://doi.org/10.1680/geot.9.P.019.

Downloaded by [] on [30/05/24]. Published with permission by the ICE under the CC-BY license